



Manipulating topological properties in $\text{Bi}_2\text{Se}_3/\text{BiSe}$ /transition metal dichalcogenide heterostructures with interface charge transfer

Xuance Jiang ^{1,2}, Turgut Yilmaz,³ Elio Vescovo,³ and Deyu Lu ^{2,*}

¹*Department of Physics and Astronomy, Stony Brook University, Stony Brook, New York 11794, USA*

²*Center for Functional Nanomaterials, Brookhaven National Laboratory, Upton, New York 11973, USA*

³*National Synchrotron Light Source II, Brookhaven National Laboratory, Upton, New York 11973, USA*



(Received 21 November 2023; revised 15 February 2024; accepted 20 February 2024; published 8 March 2024)

Heterostructures of the topological insulator Bi_2Se_3 on transition metal dichalcogenides (TMDCs) offer a new materials platform for studying novel quantum states by exploiting the interplay among topological orders, charge orders, and magnetic orders. The diverse interface attributes, such as the material combination, charge rearrangement, defects, and strain, can be utilized to manipulate the quantum properties of this class of materials. Recent experiments with $\text{Bi}_2\text{Se}_3/\text{NbSe}_2$ heterostructures show signatures of strong Rashba band splitting due to the presence of a BiSe buffer layer, but the atomic level mechanism is not fully understood. We conduct first-principles studies of the $\text{Bi}_2\text{Se}_3/\text{BiSe}/\text{TMDC}$ heterostructures with five different TMDC substrates (1*T* phase VSe_2 , MoSe_2 , and TiSe_2 and 2*H* phase NbSe_2 and MoSe_2). We find significant charge transfer at both BiSe/TMDC and $\text{Bi}_2\text{Se}_3/\text{BiSe}$ interfaces driven by the work function difference, which stabilizes the BiSe layer as an electron donor. The electric field of the $\text{Bi}_2\text{Se}_3/\text{BiSe}$ interface dipole breaks the inversion symmetry in the Bi_2Se_3 layer, leading to the giant Rashba band splitting in two quintuple layers and the recovery of the Dirac point in three quintuple layers, with the latter otherwise occurring only in thicker samples with at least six Bi_2Se_3 quintuple layers. In addition, we find that strain can significantly affect the charge transfer at the interfaces. Our study presents a promising avenue for tuning topological properties in heterostructures of two-dimensional materials, with potential applications in quantum devices.

DOI: [10.1103/PhysRevB.109.115112](https://doi.org/10.1103/PhysRevB.109.115112)

I. INTRODUCTION

Topological insulators (TIs) [1–4] are materials that are insulating in the bulk but conducting on the surface. The Dirac surface states (DSSs) of TIs are protected by time-reversal symmetry and exhibit a characteristic spin-momentum locking with a linear dispersion relation. These properties make TIs attractive for various applications in spintronics [5], quantum computing [6], optoelectronics [7,8], and thermoelectrics [9,10]. The interplay among topological orders, charge orders (e.g., superconductivity and charge density waves), and magnetic orders can create exotic quantum states, which has drawn great interest in recent research [11–16].

Heterostructures of two-dimensional (2D) materials or thin films bounded by van der Waals (vdW) forces are a fascinating playground for realizing new quantum materials. In particular, interface properties, such as the combination of materials, defects, strain, and charge rearrangement, provide a wide, tunable design space to achieve new quantum properties [17–19]. In this study, we demonstrate that interface charge transfer in vdW heterostructures can be used to tune DSSs of TIs, as shown in the schematics in Fig. 1.

In bulk TIs, the top and bottom DSSs are degenerate in energy but isolated in real space [Fig. 1(a)]. However, in thin film TIs, the DSSs can couple and open a gap [20] [Fig. 1(b)]. In

the bulk to 2D transition, the Dirac points and the corresponding spin-momentum locking are destroyed, which limits the application of thin film TIs in quantum information science. We propose to separate the top and bottom DSSs in thin film TIs in the energy domain by applying an out-of-plane electric field, which could arise from an interface dipole layer as a result of charge transfer. The electric field creates a potential energy offset in the two DSSs, which can still couple and open a gap. Two Dirac points reemerge at different energies as a result of the inversion symmetry breaking and the strong Rashba spin-orbit coupling (SOC) in thin film TIs [Fig. 1(c)]. In this study, we focus on the realization of this mechanism using bismuth selenide (Bi_2Se_3) and transition metal dichalcogenide (TMDC) heterostructures.

Bi_2Se_3 is one of the most studied three-dimensional (3D) TIs [21–23]. It has a layered structure consisting of quintuple layers (QLs) of Se-Bi-Se-Bi-Se atoms that are weakly bounded by vdW forces [Figs. 2(a) and 2(b)]. Zhang *et al.* reported that the DSS disappears when Bi_2Se_3 thin films have fewer than 6 QLs [20], as the top and bottom DSSs couple and open a gap.

TMDCs are two-dimensional materials that have diverse electronic and optical properties, such as semiconducting, metallic, and superconducting behaviors [24–28]. Monolayer TMDCs have two types of structures: the mirror-symmetric 2*H* phase and inversion-symmetric 1*T* phase, as shown in Figs. 2(c)–2(f). When Bi_2Se_3 is grown on TMDCs, novel topological properties can emerge, depending on the

*dlu@bnl.gov

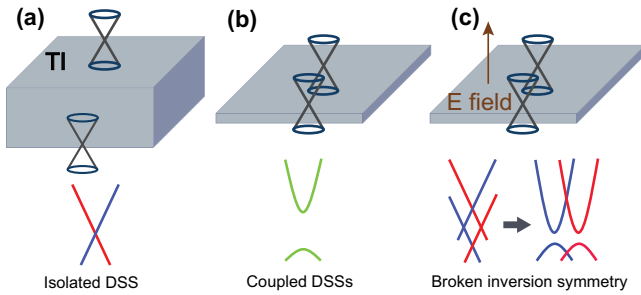


FIG. 1. Schematic of topological insulators under the spatial confinement and external electric field (top) and the impact on the surface states (bottom). (a) Bulk topological insulator with two DSSs at the top and bottom surfaces. Red and blue lines indicate different spin polarizations. (b) Thin topological insulator, where two DSSs couple and open a gap. Green lines indicate the spin-degenerate conduction and valence bands. (c) Thin topological insulator under an out-of-plane electric field. The bottom and top DSSs are separated in energy by the electric field without (left; two crosses) and with (right; gapped bands with large spin-orbit coupling) the DSSs coupling.

interlayer coupling and the band alignment between the two materials.

Recent x-ray reflectivity and x-ray diffraction studies by Choffel *et al.* showed that when Bi_2Se_3 is grown on metallic TMDCs, such as the $2H$ phase of NbSe_2 ($2H\text{-NbSe}_2$) and $1T$ phase of TiSe_2 ($1T\text{-TiSe}_2$), VSe_2 ($1T\text{-VSe}_2$), and MoSe_2 ($1T\text{-MoSe}_2$), a buffer BiSe layer can form between them [29,30]. Angle-resolved photoemission spectroscopy (ARPES) measurements revealed that the topological Dirac states reappear in the $\text{Bi}_2\text{Se}_3/\text{BiSe}/\text{NbSe}_2$ heterostructure when the thickness of Bi_2Se_3 is only 3 QLs, accompanied by a giant Rashba band splitting [31], in contrast to the critical

thickness of 6 QLs on the SiC substrate [20]. In addition, a giant Rashba splitting is found in Bi_2Se_3 bands [31].

It has been suggested that the formation of the BiSe buffer layer is responsible for the observed novel topological properties in the $\text{Bi}_2\text{Se}_3/\text{BiSe}/\text{NbSe}_2$ heterostructure. The BiSe buffer layer, similar to PbSe and LaSe, belongs to a rocksalt-structured family that can form misfit layered compounds [32–39] with TMDCs, including $1T\text{-TiSe}_2$, $2H\text{-NbSe}_2$, and $1T\text{-VSe}_2$. It has unique electronic properties such as one-dimensional electronic states [40]. More importantly, the misfit structure suppresses interlayer bonding while allowing charge transfer to dope neighboring layers and tune quantum states in the heterostructure. For example, the charge transfer between misfit layers has a strong impact on the charge density wave and superconductivity phase [41,42].

The structure of the BiSe monolayer is shown in Figs. 2(g) and 2(h). The isolated system is metallic with occupied anti-bonding states and thus tends to donate electrons to adjacent materials as in misfit materials $(\text{BiSe})_{1+\delta}/\text{NbSe}_2$ [43]. This property makes it a great candidate for modifying the electronic properties of the interface. In addition, monolayer BiSe has a flexible structure that can grow on substrates with varying lattice constants. Scanning tunneling microscopy studies of the $\text{Bi}_2\text{Se}_3/\text{BiSe}/\text{NbSe}_2$ heterostructure show that the BiSe buffer layer has a distorted square lattice with the in-plane Se-Bi-Se bond angle [θ in Fig. 2(h)] becoming either acute or obtuse [44]. Density functional theory (DFT) calculations suggest that the isolated BiSe monolayer breaks the fourfold rotation symmetry [45] characterized by two different lattice parameters (a and b), as shown in Fig. 2(g).

In spite of their intriguing topological properties, the atomic level structural details and the electronic structure of $\text{Bi}_2\text{Se}_3/\text{BiSe}/\text{TMDC}$ heterostructures are not fully understood. Due to the lattice mismatch in the three materials, a large supercell with hundreds of atoms is needed to minimize the artificial strain when building the heterostructure, which requires significant computational power. Existing *ab initio* studies of $\text{Bi}_2\text{Se}_3/\text{BiSe}/\text{NbSe}_2$ heterostructures consider an incomplete structure model, which contains only the $\text{Bi}_2\text{Se}_3/\text{BiSe}$ interface [31]. In order to qualitatively reproduce the Rashba splitting in Bi_2Se_3 , this model requires a prematurely terminated relaxation to avoid unphysical structure distortion in the absence of the NbSe_2 layer [31] since the NbSe_2 layer can play a crucial role in stabilizing the BiSe buffer layer. As such, a complete atomic-scale physical picture of $\text{Bi}_2\text{Se}_3/\text{BiSe}/\text{TMDC}$ heterostructures is still missing, and first-principles studies of the complete heterostructure are essential to gain insight into the atomic structure of the top and bottom interfaces, charge transfer characteristics, band alignment, and topological properties of $\text{Bi}_2\text{Se}_3/\text{BiSe}/\text{TMDC}$ heterostructures.

In this study, we build a series of $\text{Bi}_2\text{Se}_3/\text{BiSe}/\text{TMDC}$ models and conduct first-principles studies to reveal the origin of the giant Rashba splitting and Dirac crossing in few-QL Bi_2Se_3 . We systematically investigate five hexagonal TMDC substrates [two $2H$ phase TMDCs, $2H\text{-NbSe}_2$ and $2H\text{-MoSe}_2$, and three $1T$ phase TMDCs, $1T\text{-TiSe}_2$, $1T\text{-VSe}_2$, and $1T\text{-MoSe}_2$; see Figs. 2(c)–2(f)] that have been reported in the experimental studies of new misfit compounds [29,30] and Rashba superconductivity pairing [31]. Due to the rich

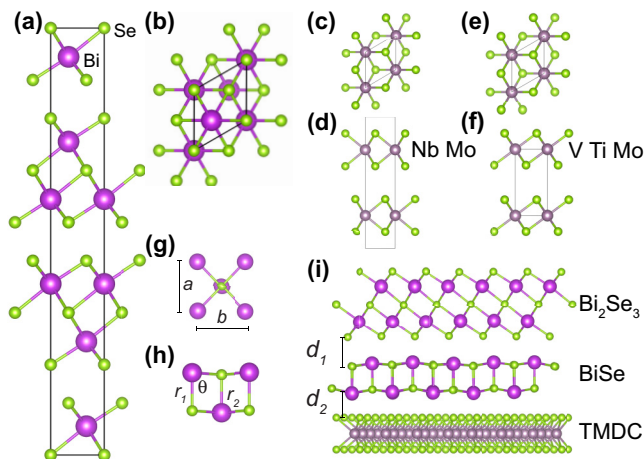


FIG. 2. (a) Side and (b) top views of the bulk Bi_2Se_3 in the conventional cell indicated by the black rectangle. (c) Top and (d) side views of $2H$ phase TMDCs. (e) Top and (f) side views of $1T$ phase TMDCs. (g) Top and (h) side views of the BiSe monolayer. (i) Side view of the $\text{Bi}_2\text{Se}_3/\text{BiSe}/\text{TMDC}$ heterostructure. The TMDC structure is taken from NbSe_2 . d_1 and d_2 are the interlayer distances of the top and bottom interfaces. Purple: Bi; light green: Se; light purple: transition metals.

TABLE I. Supercells used in the $\text{Bi}_2\text{Se}_3/\text{BiSe}/\text{TMDC}$ heterostructures.

	TMDC	BiSe	Bi_2Se_3
$2H\text{-NbSe}_2$	$\sqrt{13} \times \sqrt{39} \times 1$	$3 \times 5 \times 1$	$3 \times 3\sqrt{3} \times 1$
$1T\text{-TiSe}_2$	$7 \times 7 \times 1$	$\sqrt{34} \times \sqrt{34} \times 1$	$6 \times 6 \times 1$
$X\text{Se}_2^a$	$\sqrt{57} \times \sqrt{57} \times 1$	$\sqrt{34} \times \sqrt{34} \times 1$	$6 \times 6 \times 1$

^a $X\text{Se}_2$ represents $1T\text{-VSe}_2$ and $1T$ or $2H$ phase MoSe_2 .

electronic properties of TMDCs and the tunable strong Rashba SOC induced in Bi_2Se_3 , $\text{Bi}_2\text{Se}_3/\text{BiSe}/\text{TMDC}$ heterostructures are promising material platforms for future quantum applications, such as realizing topological superconductors and performing topological quantum computing.

The rest of this paper is organized as follows. In Sec. II, we summarize the computational details. In Sec. III A, we discuss the band alignment based on the work functions or electron affinity of heterostructure constituents. Then in Sec. III B, we analyze the structure and stability of the BiSe buffer layer. In Sec. III C, we quantify the amount of charge transfer at the interfaces. In Sec. III D, we compare the calculated band structure of $n\text{-QL } \text{Bi}_2\text{Se}_3/\text{BiSe}/\text{NbSe}_2$ ($n = 1, 2, \text{ and } 3$) with ARPES measurements. Finally, we investigate the strain effect in Sec. III E.

II. METHODS

DFT calculations are performed using the projector augmented-wave method [46] implemented in the Vienna *Ab initio* Simulation Package (VASP) [47–49]. The exchange-correlation effects are treated under the generalized gradient approximation (GGA) using the Perdew-Burke-Ernzerhof (PBE) functional [50]. The nonlocal vdW interaction is modeled by the vdW-D2 method [51].

Due to the lattice mismatch at the TMDC/BiSe and BiSe/ Bi_2Se_3 interfaces, slab models of the heterostructures are built from supercells with 300 to 600 atoms as summarized in Table I (see also Fig. 2(i) and the Supplemental Material [52]). The heterostructure models contain a TMDC monolayer, a BiSe monolayer, and 1 to 3 QLs of Bi_2Se_3 . Except when explicitly mentioned otherwise, 2-QL Bi_2Se_3 is used throughout this study. The lattice mismatch in the supercell is less than 1.5% between TMDC and Bi_2Se_3 and less than 4% between BiSe and Bi_2Se_3 . To avoid the spurious interaction between periodic images of the slab, we include a vacuum region of at least 20 Å and apply the dipole correction [53] in the DFT calculations. The structure relaxation is performed by fixing the monolayer TMDC substrate and relaxing the rest of the system until the total energy difference is less than 10^{-5} eV and the force is less than 0.01 eV/Å.

To study the interface charge transfer, the electron density difference is calculated by subtracting the electron densities of isolated TMDCs, BiSe, and Bi_2Se_3 from that of the heterostructure. The isosurface plots are generated with the VASPKIT package [54]. The band structures of the heterostructures are computed including SOC and unfolded to the Bi_2Se_3 Brillouin zone using the VASPBANDUNFOLDING package [55].

We have verified that the topological properties identified in our PBE calculations are robust against the choice

of the DFT methods, such as DFT + U [56] and the meta-GGA r2SCAN functional [57], which is an enhanced strongly constrained and appropriately normed exchange-correlation functional.

III. RESULTS AND DISCUSSION

A. Band alignment of the $\text{Bi}_2\text{Se}_3/\text{BiSe}/\text{TMDC}$ heterostructures

The freestanding BiSe monolayer [see Figs. 2(g) and 2(h)] is unstable because of the strong Coulomb repulsion from the excess electrons on the Bi atom (one per Bi atom). Our Bader charge analysis [58] shows that each Bi atom in BiSe has 0.3 electron more than that in bulk Bi_2Se_3 . As a result, the isolated BiSe monolayer favors the zigzag shape in the lateral direction rather than the rectangular shape [as shown from the side view in Fig. 2(h)] in order to maximize the Bi-Bi distance, with the Se-Bi-Se bond angle $\theta = 87^\circ$ and the out-of-plane BiSe bond length $r_1 = r_2 = 2.92$ Å. Due to the breaking of the four-fold rotation symmetry [33], in-plane parameters ($a = 4.44$ Å and $b = 4.13$ Å) have different values [see Fig. 2(g)]. One practical strategy to stabilize the BiSe monolayer is to put it in contact with electron acceptors forming heterostructures [43]. Since the energy level alignment at the interface plays a critical role in determining the charge rearrangement and the thermodynamic stability of the heterostructures, below we investigate the energy level alignment at the BiSe/TMDC and $\text{Bi}_2\text{Se}_3/\text{BiSe}$ interfaces.

We calculate the work function W of the isolated monolayer BiSe and metallic monolayer TMDCs, as well as the electron affinity E_a of the isolated semiconducting monolayer TMDC and bulk Bi_2Se_3 , as shown in Table II. At the PBE level, $W_{\text{BiSe}} = 3.72$ eV, which is lower than that of all the metallic monolayer TMDCs, $1T\text{-MoSe}_2$ (4.52 eV), $1T\text{-VSe}_2$ (5.01 eV), $1T\text{-TiSe}_2$ (5.31 eV), and $2H\text{-NbSe}_2$ (5.52 eV), and E_a of the semiconducting $2H\text{-MoSe}_2$ monolayer (3.90 eV). Our results show good agreement with the PBE calculations in the literature, e.g., $2H\text{-NbSe}_2$ (5.54 eV [59]), $1T\text{-TiSe}_2$ (5.35 eV [60]), $1T\text{-VSe}_2$ (5.05 eV [60]), $1T\text{-MoSe}_2$ (4.58 eV [60]), and $2H\text{-MoSe}_2$ (3.86 eV [61]). They are in reasonable agreement with the measured W of the $1T\text{-VSe}_2$ monolayer (5.0 eV [62] and 5.52 eV [63]) and E_a of the semiconducting $2H\text{-MoSe}_2$ monolayer (3.5 and 3.8 eV [64]).

Based on Table II, at the BiSe/TMDC interface, W_{TMDC} or E_a^{TMDC} is larger than W_{BiSe} by up to 1.80 eV, which drives electron transfer from BiSe to TMDCs. At the $\text{Bi}_2\text{Se}_3/\text{BiSe}$ interface, W_{BiSe} is lower than $E_a^{\text{Bi}_2\text{Se}_3}$ by 1.68 eV. Therefore, BiSe also donates electrons to Bi_2Se_3 . The charge transfer at both the top and bottom interfaces can significantly reduce the Coulomb repulsion of excess electrons in BiSe, which in turn can stabilize the BiSe buffer layer.

The charge transfer in the $\text{Bi}_2\text{Se}_3/\text{BiSe}/\text{TMDC}$ heterostructures creates interface dipoles at both the top and bottom interfaces. The resulting dipole field shifts the vacuum potential, which determines the overall band alignment in the heterostructures. A qualitative picture is outlined in Fig. 3. As illustrated in this diagram, the band alignment at the BiSe/TMDC and $\text{Bi}_2\text{Se}_3/\text{BiSe}$ interfaces is dominated by dipole potentials ΔV_2 and ΔV_1 , respectively. The relative position of the conduction band minimum (CBM) of

TABLE II. Work functions (eV) of the metallic monolayer TMDCs ($2H$ -NbSe₂, $1T$ -TiSe₂, $1T$ -VSe₂, and $1T$ -MoSe₂) and BiSe and electron affinities (eV) of the semiconducting monolayer TMDC ($2H$ -MoSe₂) and 2-QL Bi₂Se₃. Values in the parentheses are taken from the literature.

	TMDCs					BiSe	Bi ₂ Se ₃
	$2H$ -NbSe ₂	$1T$ -TiSe ₂	$1T$ -VSe ₂	$1T$ -MoSe ₂	$2H$ -MoSe ₂		
DFT	5.52 (5.54 ^a)	5.31(5.35 ^b)	5.01(5.05 ^b)	4.52(4.58 ^b)	3.90 (3.86 ^c)	3.72	5.40
Experiment			5.0 ^d , 5.52 ^e		3.5, 3.8 ^f		

^aSee Ref. [59].

^bSee Ref. [60].

^cSee Ref. [61].

^dSee Ref. [62].

^eSee Ref. [63].

^f(3.8±0.1) eV on Al₂O₃/Si and (3.5±0.1) eV on SiO₂/Si. See Ref. [64].

Bi₂Se₃ (ΔE) versus the Fermi level is associated with ΔV_1 through $\Delta E = W_{\text{BiSe}} - E_a^{\text{Bi}_2\text{Se}_3} - \Delta V_1$. We plot the Hartree potential of the 2-QL Bi₂Se₃/BiSe/NbSe₂ heterostructure in Fig. S3 of the Supplemental Material [52]. The vacuum level difference of 0.33 eV between the bottom and top of the heterostructure corresponds to $\Delta V_2 - \Delta V_1$, as the net effect of the interface dipole. From the projected density of states (PDOS) of the Bi₂Se₃ bands, ΔE is estimated to be 0.44 eV. We note that W and E_a in the heterostructure (as shown in Fig. 3) can be slightly different from those of the isolated system due to structure distortion and charge rearrangement. For example, in 2-QL Bi₂Se₃/BiSe/NbSe₂, Bi₂Se₃ has a slightly larger (by 3%) $E_a^{\text{Bi}_2\text{Se}_3}$ than the freestanding system.

B. Structure and stability of the BiSe buffer layer

Compared to the freestanding BiSe monolayer, the out-of-plane Bi-Se bond lengths (r_1 and r_2) are about 5% shorter in the fully relaxed heterostructures [see Fig. 2(i) and Table III]. Unlike other misfit structures [43], the BiSe monolayer in Bi₂Se₃/BiSe/TMDC heterostructures can have significant structure distortion (i.e., $r_1 \neq r_2$), which breaks the inversion symmetry. The degree of this distortion depends on the relative energy level alignment on the top and bottom interfaces. At the top interface, $\Delta_T = E_a^{\text{Bi}_2\text{Se}_3} - W_{\text{BiSe}} = 1.68$ eV is the driving force of electron donation from BiSe to Bi₂Se₃. Similarly, at the bottom interface, $\Delta_B = W_{\text{TMDC}}(E_a^{\text{TMDC}}) - W_{\text{BiSe}}$ causes electrons to flow from BiSe to the TMDC. Larger charge transfer results in stronger coupling at the interface,

which will pull Bi atoms out of the Se plane in BiSe. Therefore, the ratio $\eta = \Delta_B/\Delta_T$ can be used to qualitatively determine the degree of asymmetry of the BiSe monolayer. For example, in Bi₂Se₃/BiSe/NbSe₂, η has the largest value of 1.07. As a result, Bi atoms in the top surface of BiSe move towards Bi₂Se₃ by 0.28 Å relative to the top Se plane, while Bi atoms in the bottom surface move towards NbSe₂ by 0.38 Å relative to the bottom Se plane. Consequently, $r_2 = 2.84$ Å is longer than $r_1 = 2.75$ Å by 3%. In Bi₂Se₃/BiSe/ $1T$ -MoSe₂ with a moderate η of 0.48, the BiSe layer is almost inversion symmetric, as r_2 is longer than r_1 by only 0.7%. The trend is completely reversed in Bi₂Se₃/BiSe/ $2H$ -MoSe₂ with a very small η of 0.11, where $r_2 = 2.75$ Å is shorter than $r_1 = 2.82$ Å by 2.5%.

The coupling strength at the interface can also be characterized by interlayer distances d_1 and d_2 at the top and bottom interfaces, respectively, as shown in Fig. 2(i). From Table III, we can see that as Δ_B decreases, d_2 increases from 2.92 to 3.27 Å, implying weaker interactions. On the other hand, d_1 shows a mild opposite trend, decreasing from 3.08 to 2.98 Å. This suggests that stronger interaction at the BiSe/TMDC interface slightly weakens the interaction at the Bi₂Se₃/BiSe interface. This trend is consistent with detailed charge transfer analysis in Sec. III C.

In the bottom-up growth of heterostructures (e.g., using molecular-beam epitaxy), the adhesive energy of the BiSe/TMDC interface is a crucial factor of the thermodynamic stability. We calculate the adhesive energy for each TMDC substrate,

$$\varepsilon_{\text{adh}}^{\text{BiSe/TMDC}} = (E_{\text{BiSe/TMDC}} - n\varepsilon_{\text{BiSe}} - m\varepsilon_{\text{TMDC}}), \quad (1)$$

where $E_{\text{BiSe/TMDC}}$ and $\varepsilon_{\text{BiSe}}$ and $\varepsilon_{\text{TMDC}}$ are the energies of the BiSe/TMDC interface and individual components per unit cell, respectively. n and m are the corresponding numbers of BiSe and TMDC 2D unit cells in the heterostructure supercell. The results in Table III show that as W_{TMDC} increases, $\varepsilon_{\text{adh}}^{\text{BiSe/TMDC}}$ becomes more negative from -2.82 eV ($1T$ -MoSe₂) to -3.98 eV ($2H$ -NbSe₂) per BiSe chemical formula, as a result of stronger charge transfer and coupling between BiSe and TMDC substrates. However, for the semiconducting $2H$ -MoSe₂ substrate, $\Delta_B = 0.18$ eV is very small. This implies a much weaker charge transfer, and the resulting $\varepsilon_{\text{adh}}^{\text{BiSe/TMDC}} = -1.82$ eV is the smallest among the five

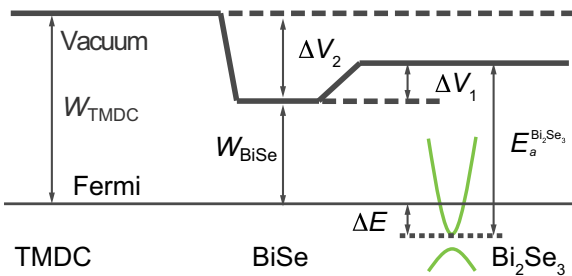


FIG. 3. Band alignment diagram of Bi₂Se₃/BiSe/TMDC heterostructures. The thick solid line, thin solid line, and green curves represent the vacuum level, Fermi level, and Bi₂Se₃ bands, respectively.

TABLE III. Structural parameters of the relaxed 2-QL $\text{Bi}_2\text{Se}_3/\text{BiSe}/\text{TMDC}$ heterostructures (r_1 , r_2 , d_1 , and d_2 , in Å) and the adhesive energy of the BiSe/TMDC interface ($\epsilon_{\text{BiSe}/\text{TMDC}}^{\text{adh}}$, in eV). r_1 and r_2 are the average out-of-plane Bi-Se bond lengths in the BiSe monolayer. In the freestanding BiSe monolayer, $r_1 = r_2 = 2.92$ Å. d_1 (d_2) is the interlayer distance at the top (bottom) interface.

	TMDC				
	$2H\text{-NbSe}_2$	$1T\text{-TiSe}_2$	$1T\text{-VSe}_2$	$1T\text{-MoSe}_2$	$2H\text{-MoSe}_2$
r_1	2.75	2.79	2.77	2.80	2.82
r_2	2.84	2.84	2.82	2.82	2.75
d_1	3.08	3.06	3.08	3.05	2.98
d_2	2.92	3.06	3.12	3.15	3.27
$\epsilon_{\text{BiSe}/\text{TMDC}}^{\text{adh}}$	-3.98	-2.80	-3.03	-2.82	-1.82

TMDCs. Our adhesive energy calculations suggest that a BiSe buffer layer can preferably grow on metal TMDC substrates with large work functions, which is in line with experimental observations [29].

C. Interface charge transfer

We examine the electronic properties of two interfaces in $\text{Bi}_2\text{Se}_3/\text{BiSe}/\text{TMDC}$ and determine the amount of charge transfer. In Fig. 4(a), we plot the isosurface of the electron density difference between the combined system and its individual components. One can clearly see that the electron flows out of Bi p_z orbitals in BiSe (yellow green blobs) into Se p_z orbitals in either TMDC or Bi_2Se_3 (pink blobs).

The plane-averaged electron density difference plot of the heterostructure is shown in Fig. 4(b) (top panel), where significant charge transfer occurs from the BiSe buffer layer (negative regions) to both NbSe_2 and Bi_2Se_3 (positive regions). To quantify the amount of charge transfer at the two interfaces, we integrate the plane-averaged electron density difference along the surface normal direction to obtain the cumulative charge profile, as shown in Fig. 4(b) (bottom panel). Two pronounced peaks are indicated by the vertical red lines, corresponding to the net amount of charge transfer on each interface. The positive peak at the bottom interface corresponds to electron donation to NbSe_2 with $\delta q_2 = 0.06e^-$, and the negative peak at the top interface corresponds to electron donation to Bi_2Se_3 with $\delta q_1 = 0.04e^-$.

The trend of the charge transfer with respect to W (E_a) is shown in Fig. 4(c). As we expect, δq_2 grows monotonously with W (E_a), varying from $0.01e^-$ to $0.06e^-$. The smallest δq_2 value of $0.01e^-$ is obtained on the $2H\text{-MoSe}_2$ substrate, with $W = 0.18$ eV. On the other hand, δq_1 overall shows a mild decay trend against W (E_a), except for $2H\text{-NbSe}_2$, which has a slightly larger δq_1 ($0.037e^-$) than $1T\text{-TiSe}_2$ ($0.035e^-$). Since δq_1 is primarily determined by the constant value of Δ_T (1.68 eV), it exhibits a much narrower dynamic range from 0.035 to 0.044. Another factor that may contribute to the nonmonotonic behavior of δq_1 is the in-plane strain in the heterostructure, which will be discussed in Sec. III E. There is more tensile strain in the Bi_2Se_3 and BiSe layers in $\text{Bi}_2\text{Se}_3/\text{BiSe}/\text{NbSe}_2$ heterostructure than in $\text{Bi}_2\text{Se}_3/\text{BiSe}/\text{TiSe}_2$ (see the Supplemental Material [52]), which may cause an enhancement of δq_1 in the former and a reduction of δq_1 in the latter.

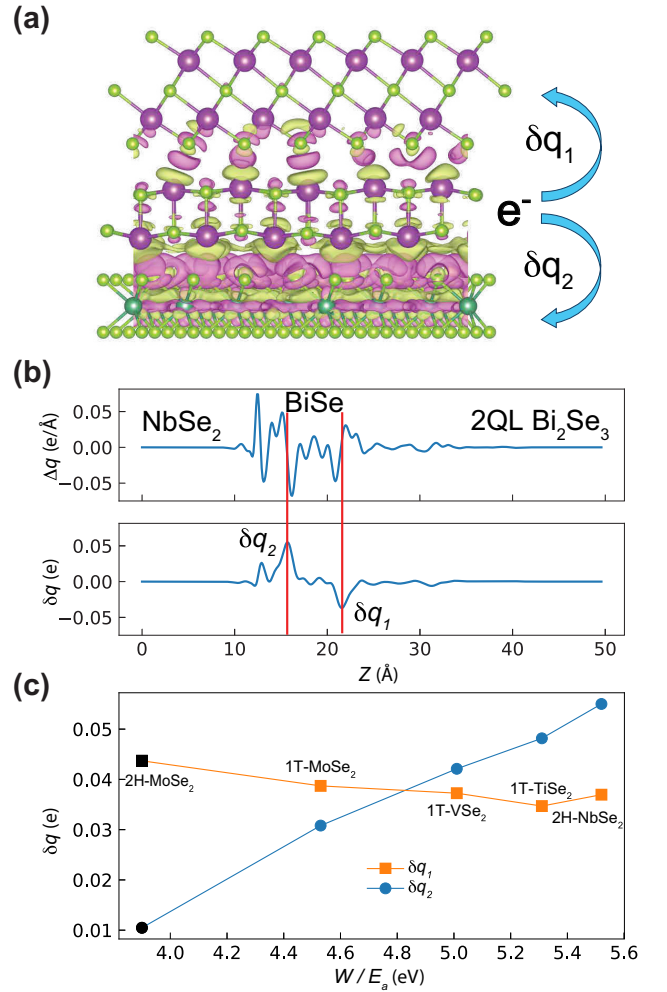


FIG. 4. (a) Isosurface plot of the electron density difference of heterostructure 2-QL $\text{Bi}_2\text{Se}_3/\text{BiSe}/\text{NbSe}_2$. For clarity, only the bottom QL of Bi_2Se_3 is shown. Pink and yellow green regions indicate the electron gain and loss, respectively. (b) Top: the plane-averaged electron density curve of 2-QL $\text{Bi}_2\text{Se}_3/\text{BiSe}/\text{NbSe}_2$. Bottom: the corresponding cumulative charge profile in units of electrons per BiSe formula. Two peaks indicated by the red lines correspond to the amount of charge transfer at two interfaces. (c) Effect of the work function or electron affinity of TMDC substrates on interface charge transfer. The black symbols correspond to semiconducting $2H\text{-MoSe}_2$.

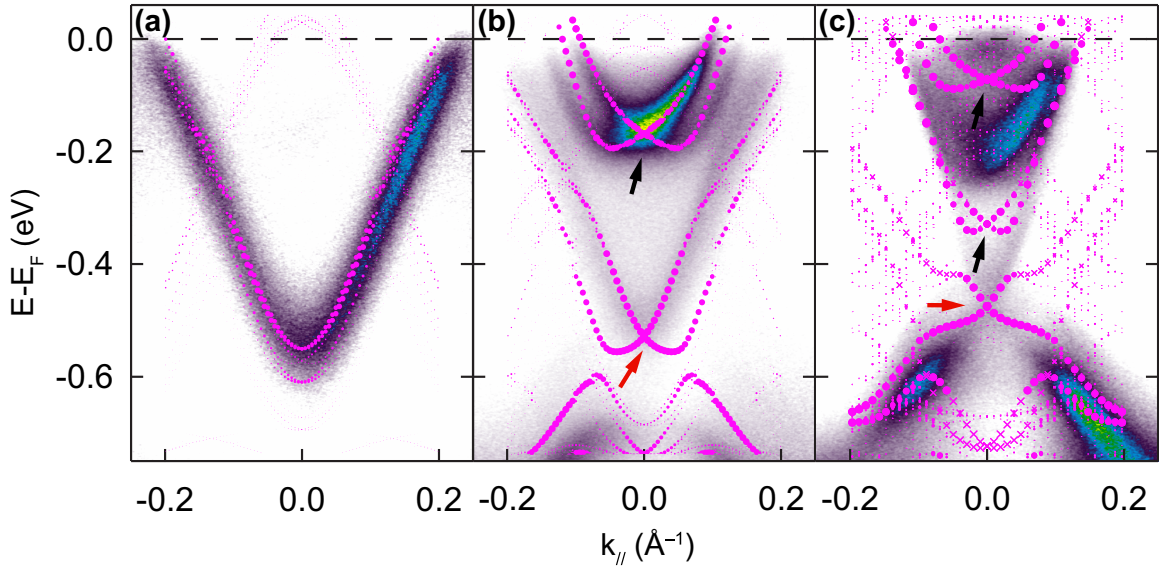


FIG. 5. Comparison between experimental [31] and DFT band structures of (a) 1-QL, (b) 2-QL, and (c) 3-QL $\text{Bi}_2\text{Se}_3/\text{BiSe}/\text{NbSe}_2$ heterostructures. The magenta circles are unfolded band structures from DFT. Black arrows indicate the QW states; red arrows indicate the Dirac points. The bottom and top QL states in (c) are indicated by crosses and circles, respectively.

D. Band structure and giant Rashba splitting

Recent ARPES measurements revealed interesting topological properties in few-layer $\text{Bi}_2\text{Se}_3/\text{BiSe}/\text{NbSe}_2$ heterostructures [31]. To understand the ARPES data, the calculated band structures (magenta dots) of the 1-QL, 2-QL, and 3-QL $\text{Bi}_2\text{Se}_3/\text{BiSe}/1\text{-ML NbSe}_2$ heterostructures are unfolded to the Brillouin zone of Bi_2Se_3 and overlaid on top of the measured band structure from Ref. [31] in Fig. 5. For this comparison, the calculated Fermi levels are slightly shifted by up to 0.15 eV to match the experiment. The amount of this adjustment is comparable to the differences in the work function between DFT and experiment, as shown in Table II.

In the 1-QL $\text{Bi}_2\text{Se}_3/\text{BiSe}/\text{NbSe}_2$ band structure [see Fig. 5(a)], ARPES shows a V-shaped conduction band derived from Bi and Se p orbitals of Bi_2Se_3 , which is reproduced very well by our DFT calculations. The Bi_2Se_3 CBM is lower than the Fermi level by 0.55 eV, which is qualitatively reproduced by 0.70 eV from DFT. The valence band of Bi_2Se_3 is at lower energies outside the range of Fig. 5(a).

In 2-QL $\text{Bi}_2\text{Se}_3/\text{BiSe}/\text{NbSe}_2$, the surface states in Bi_2Se_3 are gapped, and the CBM shows a band splitting near the Γ point, indicated by the red arrow [see Fig. 5(b)]. Due to the charge transfer between BiSe and Bi_2Se_3 , the negative interface dipole along the out-of-plane direction breaks the inversion symmetry, which separates the DSSs in energy and weakens their coupling. The DFT band structure qualitatively reproduces both the band gap and band splitting at the CBM, consistent with the schematic diagram in Fig. 1(c). The underestimated gap and overestimated surface band splitting in DFT, compared to experiment, are likely due to the limitation of the DFT method, which may not capture the screened long-range Coulomb repulsion between top and bottom surface states accurately [65].

Notably, we observe the giant Rashba band splitting in the quantum well (QW) state indicated by the black arrow,

which is strong evidence of the dipole-induced giant Rashba SOC effect. In contrast, the QW state in the $\text{Bi}_2\text{Se}_3/\text{NbSe}_2$ band structure (i.e., without the BiSe buffer layer) resembles the pristine 2-QL Bi_2Se_3 with negligible Rashba splitting (see Fig. S2 in the Supplemental Material [52]). The Rashba constant is defined as $\alpha_R = 2\Delta E/\Delta k$, where ΔE and Δk are energy and momentum splitting values. Based on the ARPES measurement, $\Delta E = 0.019$ eV, and $\Delta k = 0.038 \text{ \AA}^{-1}$, which yield $\alpha_R = 1.0 \text{ eV \AA}$ [31]. Values of ΔE , Δk , and α_R from simulated band structures of 2-QL $\text{Bi}_2\text{Se}_3/\text{BiSe}/\text{NbSe}_2$ heterostructures are listed in Table IV. In the heterostructure without strain, $\alpha_R = 1.1 \text{ eV \AA}$ is in excellent agreement with experiment. Note that the Au(111) surface, as a typical giant Rashba SOC material, has a Rashba constant of 0.33 eV \AA [66], and bulk BiTeI, among the highest Rashba SOC materials, has a Rashba constant of 3.8 eV \AA [67].

When the thickness of Bi_2Se_3 in the heterostructure increases to 3 QLs, the Dirac point reappears, as indicated by the red arrow in Fig. 5(c), which is clearly reproduced by DFT. This feature is due to both the spatial separation of the top and bottom surface states and their energy offset, caused by the interface dipole field. In fact, the interface electric field pulls the bottom surface state down into the bulk states, so the coupling between the top and bottom surface states is weaker than the freestanding 3-QL Bi_2Se_3 . In contrast, in pristine Bi_2Se_3 thin films the surface Dirac point appears only when the thickness is equal to or more than 6 QLs. In addition to the surface Dirac point, at higher energies, ARPES data also exhibit two QW states with giant Rashba band splitting. These QW states are reproduced by DFT calculations (indicated by black arrows), while the energy positions in DFT are closer to the Dirac point than the experiment by 0.09 eV, likely due to the limitation of the PBE functional. In Fig. 5(c), we distinguish the quasiparticle states dominated by the bottom and top QLs with crosses and dots, respectively. The

TABLE IV. Rashba strength parameter of different 2-QL $\text{Bi}_2\text{Se}_3/\text{BiSe}/\text{TMDC}$ heterostructures.

	TMDCs					Expt. ^a
	$2H\text{-NbSe}_2$	$1H\text{-TiSe}_2$	$1T\text{-VSe}_2$	$1T\text{-MoSe}_2$	$2H\text{-MoSe}_2$	$2H\text{-NbSe}_2$
α_R (eV Å)	1.1	1.0	1.1	1.1	1.2	1.0

^aSee Ref. [31].

bottom-QL-dominated states do not appear in the experimental band structure, likely due to the thickness sensitivity of the ARPES measurement.

Overall, our calculations reproduce well all the key topological features in the ARPES measurement of few-layer $\text{Bi}_2\text{Se}_3/\text{BiSe}/\text{NbSe}_2$ heterostructures, and the calculated giant Rashba constant is in excellent agreement with the experiment.

In Table IV, we compare α_R of different TMDC heterostructures based on the band splitting of the first QW state in 2-QL $\text{Bi}_2\text{Se}_3/\text{BiSe}/\text{TMDC}$. The calculated α_R are between 1.0 eV \AA ($1T\text{-TiSe}_2$) and 1.2 eV \AA ($2H\text{-MoSe}_2$). Note that α_R of the $2H\text{-MoSe}_2$ heterostructure is 9% larger than that of the $2H\text{-NbSe}_2$ heterostructure, which is consistent with the charge transfer analysis, as larger δq_1 induces larger Rashba splitting.

E. Effect of strain

The dipole field from the $\text{Bi}_2\text{Se}_3/\text{BiSe}$ interface is the critical factor that leads to the novel topological properties in the $\text{Bi}_2\text{Se}_3/\text{BiSe}/\text{TMDC}$ heterostructures. Therefore, it is advantageous to have the ability to tune δq_1 in order to enhance this dipole field, combined with a large enough δq_2 to stabilize the BiSe buffer layer. As shown in Fig. 4(c), the range of δq_1 is about $0.0027e^-$ among the TMDCs (between $1T\text{-MoSe}_2$, which has a small work function, and $2H\text{-NbSe}_2$, which has a large work function) that can grow the BiSe layer in experiment [29]. Here we consider strain as another means to control the interface charge transfer.

Strain can have significant effects on the electronic properties of 2D materials. Specifically, we investigate the effect of strain on the charge transfer at the two interfaces. We use the 2-QL $\text{Bi}_2\text{Se}_3/\text{BiSe}/\text{NbSe}_2$ heterostructure as an exemplary system and apply a uniform in-plane strain between -1% and $+1\%$ to mimic the strain induced by the lattice mismatch between TMDCs and their substrate. We find that tensile strain enhances the charge transfer at the $\text{Bi}_2\text{Se}_3/\text{BiSe}$ interface, while compressive strain suppresses it, as shown in Fig. 6(c). In fact, 1% tensile strain increases δq_1 by $0.0029e^-$, which is slightly larger than the effect ($0.0027e^-$) caused by different TMDCs. As a result, heterostructures under tensile strain have larger Rashba splitting, as shown in Fig. 6(b). The calculated α_R increases as a function of strain: $\alpha_R = 1.0, 1.1$, and 1.4 eV \AA under 1% compressive strain, zero strain, and 1% tensile strain, respectively. On the other hand, 1% tensile strain increases δq_2 by $0.0015e^-$, which is much smaller than the effects of different TMDCs ($0.024e^-$).

To understand the effects of strain on charge transfer, we focus on the BiSe buffer layer and plot the PDOS of BiSe in Fig. 6(d). The in-plane tensile strain effectively stretches the in-plane Bi-Se bond and compresses the out-of-plane Bi-Se

bond in the BiSe monolayer, as shown in Fig. 6(a). Consequently, the p_x/p_y antibonding orbitals move to lower energy, and p_z antibonding orbitals move to higher energy, indicated by black arrows. Thus, the p_z electrons in BiSe become more unstable than those without strain, which enhances the charge transfer of Bi p_z electrons to neighboring layers in both upper and lower interfaces.

IV. CONCLUSION

In this work, we systematically studied a series of $\text{Bi}_2\text{Se}_3/\text{BiSe}/\text{TMDC}$ heterostructures with small lattice mismatch using first-principles calculations. With detailed analysis of the band alignment and charge transfer, we showed that the rocksalt BiSe buffer layer can donate electrons to

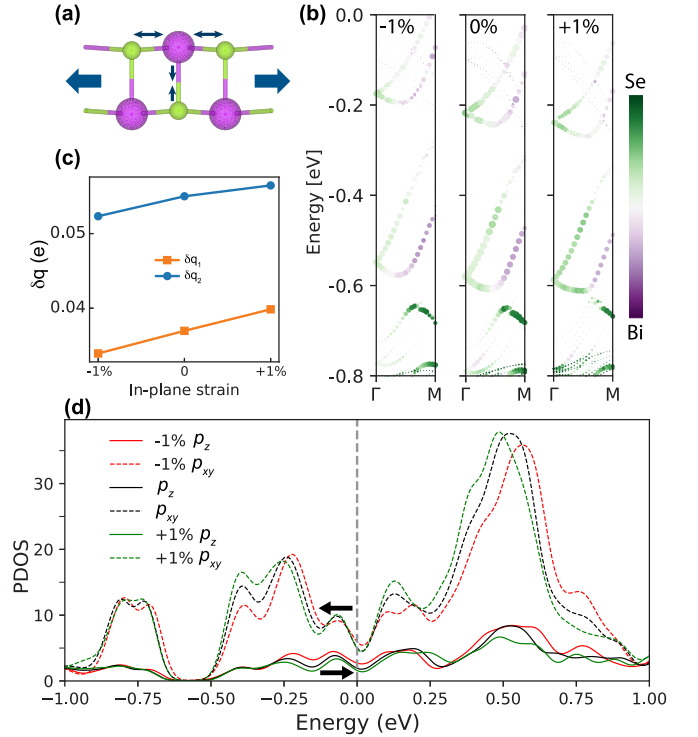


FIG. 6. (a) Illustration of the structural change in the BiSe layer in the heterostructure under the tensile strain. The large blue arrows indicate the in-plane tensile strain. The small arrows indicate the change in the bond length. (b) Band structure of $\text{Bi}_2\text{Se}_3/\text{BiSe}/\text{NbSe}_2$ under 1% compressive strain (left), zero strain (middle), and +1% tensile strain (right) projected onto Bi_2Se_3 orbitals. Purple and green indicate Bi- and Se-dominated orbitals. (c) The effect of in-plane strain on the charge transfer of the $\text{Bi}_2\text{Se}_3/\text{BiSe}/\text{NbSe}_2$ heterostructure. (d) Projected density of states of the BiSe layer under different amounts of in-plane tensile strain. Black arrows highlight the change in the projected density of states.

both Bi_2Se_3 and TMDC layers and the magnitude depends on the work function (or electron affinity) difference. We showed that TMDCs with a large work function are more favorable to stabilize the BiSe buffer layer and cause a larger amount of charge transfer on the BiSe/TMDC interface, but with a much weaker impact on the charge transfer at the $\text{Bi}_2\text{Se}_3/\text{BiSe}$ interface.

The resulting dipole at the $\text{Bi}_2\text{Se}_3/\text{BiSe}$ interface creates an out-of-plane electric field that breaks the inversion symmetry in the Bi_2Se_3 layer and introduces an energy offset to the top and bottom Dirac surface states. As a result, intriguing electronic properties emerge in few-QL Bi_2Se_3 , including giant Rashba band splitting in the quantum well states in 2-QL $\text{Bi}_2\text{Se}_3/\text{BiSe}/\text{NbSe}_2$ and the reappearance of the topologically protected Dirac point in 3-QL $\text{Bi}_2\text{Se}_3/\text{BiSe}/\text{NbSe}_2$. These results are in excellent agreement with the experimental band structure in the literature from ARPES measurements. In addition, we found that tensile strain can significantly enhance the charge transfer on both interfaces from the BiSe p_z antibonding orbitals, which provides another mechanism

to control the topological properties of $\text{Bi}_2\text{Se}_3/\text{BiSe}/\text{TMDC}$ heterostructures.

The emergence of Dirac surface states in quasi-2D materials may open a new avenue for new quantum material platforms, which require the interplay of topological states with strong proximity effects of the superconductivity or charge density wave phase.

ACKNOWLEDGMENTS

We thank Dr. C.-Z. Chang for providing the ARPES data used in this study. We thank Dr. J. Cano for the valuable discussions. This research used the Theory and Computation resources from the Center for Functional Nanomaterials (CFN) and resources of the National Synchrotron Light Source II, which are U.S. Department of Energy Office of Science User Facilities, operated for the DOE Office of Science by Brookhaven National Laboratory under Contract No. DE-SC0012704.

-
- [1] M. Z. Hasan and C. L. Kane, Colloquium: Topological insulators, *Rev. Mod. Phys.* **82**, 3045 (2010).
- [2] S. Q. Shen, *Topological Insulators*, Springer Series in Solid-State Sciences Vol. 174 (Springer, Berlin, 2012).
- [3] J. E. Moore, The birth of topological insulators, *Nature (London)* **464**, 194 (2010).
- [4] L. Fu, C. L. Kane, and E. J. Mele, Topological insulators in three dimensions, *Phys. Rev. Lett.* **98**, 106803 (2007).
- [5] Y. Fan and K. L. Wang, Spintronics based on topological insulators, *Spin* **6**, 1640001 (2016).
- [6] M. He, H. Sun, and Q. L. He, Topological insulator: Spintronics and quantum computations, *Front. Phys.* **14**, 43401 (2019).
- [7] H. Plank, S. N. Danilov, V. V. Bel'kov, V. A. Shalygin, J. Kampmeier, M. Lanius, G. Mussler, D. Grützmacher, and S. D. Ganichev, Opto-electronic characterization of three dimensional topological insulators, *J. Appl. Phys.* **120**, 165301 (2016).
- [8] A. Politano, L. Viti, and M. S. Vitiello, Optoelectronic devices, plasmonics, and photonics with topological insulators, *APL Mater.* **5**, 035504 (2017).
- [9] N. Xu, Y. Xu, and J. Zhu, Topological insulators for thermoelectrics, *npj Quantum Mater.* **2**, 51 (2017).
- [10] L. Müchler, F. Casper, B. Yan, S. Chadov, and C. Felser, *Topological Insulators*, edited by K. Koumoto and T. Mori, Thermoelectric Nanomaterials: Materials Design and Applications Vol. 182 (Springer Series in Materials Science, Berlin, 2013), pp. 123–139.
- [11] X.-L. Qi and S.-C. Zhang, Topological insulators and superconductors, *Rev. Mod. Phys.* **83**, 1057 (2011).
- [12] L. Fu and C. L. Kane, Superconducting proximity effect and Majorana fermions at the surface of a topological insulator, *Phys. Rev. Lett.* **100**, 096407 (2008).
- [13] H. Pan, M. Xie, F. Wu, and S. Das Sarma, Topological phases in AB-stacked $\text{MoTe}_2/\text{WSe}_2$: \mathbb{Z}_2 topological insulators, Chern insulators, and topological charge density waves, *Phys. Rev. Lett.* **129**, 056804 (2022).
- [14] N. Mitsuishi, Y. Sugita, M. S. Bahramy, M. Kamitani, T. Sonobe, M. Sakano, T. Shimojima, H. Takahashi, H. Sakai, K. Horiba, H. Kumigashira, K. Taguchi, K. Miyamoto, T. Okuda, S. Ishiwata, Y. Motome, and K. Ishizaka, Switching of band inversion and topological surface states by charge density wave, *Nat. Commun.* **11**, 2466 (2020).
- [15] Y. S. Hor, P. Roushan, H. Beidenkopf, J. Seo, D. Qu, J. G. Checkelsky, L. A. Wray, D. Hsieh, Y. Xia, S.-Y. Xu, D. Qian, M. Z. Hasan, N. P. Ong, A. Yazdani, and R. J. Cava, Development of ferromagnetism in the doped topological insulator $\text{Bi}_{2-x}\text{Mn}_x\text{Te}_3$, *Phys. Rev. B* **81**, 195203 (2010).
- [16] H. Wang, J. Kally, J. S. Lee, T. Liu, H. Chang, D. R. Hickey, K. A. Mkhoyan, M. Wu, A. Richardella, and N. Samarth, Surface-state-dominated spin-charge current conversion in topological-insulator-ferromagnetic-insulator heterostructures, *Phys. Rev. Lett.* **117**, 076601 (2016).
- [17] S. Thiel, G. Hammerl, A. Schmehl, C. W. Schneider, and J. Mannhart, Tunable quasi-two-dimensional electron gases in oxide heterostructures, *Science* **313**, 1942 (2006).
- [18] Y. He, Y. Yang, Z. Zhang, Y. Gong, W. Zhou, Z. Hu, G. Ye, X. Zhang, E. Bianco, S. Lei, Z. Jin, X. Zou, Y. Yang, Y. Zhang, E. Xie, J. Lou, B. Yakobson, R. Vajtai, B. Li, and P. Ajayan, Strain-induced electronic structure changes in stacked van der Waals heterostructures, *Nano Lett.* **16**, 3314 (2016).
- [19] Z. Lin, A. McCreary, N. Briggs, S. Subramanian, K. Zhang, Y. Sun, X. Li, N. J. Borys, H. Yuan, S. K. Fullerton-Shirey, A. Chernikov, H. Zhao, S. McDonnell, A. M. Lindenberg, K. Xiao, B. J. LeRoy, M. Drndić, J. C. M. Hwang, J. Park, M. Chhowalla *et al.*, 2D materials advances: from large scale synthesis and controlled heterostructures to improved characterization techniques, defects and applications, *2D Mater.* **3**, 042001 (2016).
- [20] Y. Zhang, K. He, C.-Z. Chang, C.-L. Song, L.-L. Wang, X. Chen, J.-F. Jia, Z. Fang, X. Dai, W.-Y. Shan, S.-Q. Shen, Q. Niu, X.-L. Qi, S.-C. Zhang, X.-C. Ma, and Q.-K. Xue, Crossover of the three-dimensional topological insulator Bi_2Se_3 to the two-dimensional limit, *Nat. Phys.* **6**, 584 (2010).

- [21] H. Zhang, C.-X. Liu, X.-L. Qi, X. Dai, Z. Fang, and S.-C. Zhang, Topological insulators in Bi_2Se_3 , Bi_2Te_3 and Sb_2Te_3 with a single Dirac cone on the surface, *Nat. Phys.* **5**, 438 (2009).
- [22] W. Zhang, R. Yu, H.-J. Zhang, X. Dai, and Z. Fang, First-principles studies of the three-dimensional strong topological insulators Bi_2Te_3 , Bi_2Se_3 and Sb_2Te_3 , *New J. Phys.* **12**, 065013 (2010).
- [23] K. Mazumder and P. M. Shirage, A brief review of Bi_2Se_3 based topological insulator: From fundamentals to applications, *J. Alloys Compd.* **888**, 161492 (2021).
- [24] S. Manzeli, D. Ovchinnikov, D. Pasquier, O. V. Yazyev, and A. Kis, 2D transition metal dichalcogenides, *Nat. Rev. Mater.* **2**, 17033 (2017).
- [25] W. Choi, N. Choudhary, G. H. Han, J. Park, D. Akinwande, and Y. H. Lee, Recent development of two-dimensional transition metal dichalcogenides and their applications, *Mater. Today* **20**, 116 (2017).
- [26] H. Wang, X. Huang, J. Lin, J. Cui, Y. Chen, C. Zhu, F. Liu, Q. Zeng, J. Zhou, P. Yu, X. Wang, H. He, S. H. Tsang, W. Gao, K. Suenaga, F. Ma, C. Yang, L. Lu, T. Yu, E. H. T. Teo *et al.*, High-quality monolayer superconductor NbSe_2 grown by chemical vapour deposition, *Nat. Commun.* **8**, 394 (2017).
- [27] P. Goli, J. Khan, D. Wickramaratne, R. K. Lake, and A. A. Balandin, Charge density waves in exfoliated films of van der Waals materials: Evolution of Raman spectrum in TiSe_2 , *Nano Lett.* **12**, 5941 (2012).
- [28] T. Yilmaz, X. Jiang, D. Lu, P. M. Sheverdyaeva, A. V. Matetskiy, P. Moras, F. Mazzola, I. Vobornik, J. Fujii, K. Evans-Lutterodt, and E. Vescovo, Dirac nodal arc in 1T- VSe_2 , *Communications Materials* **4**, 47 (2023).
- [29] M. A. Choffel, R. N. Gannon, F. Göhler, A. M. Miller, D. L. Medlin, T. Seyller, and D. C. Johnson, Synthesis and electrical properties of a new compound $(\text{BiSe})_{0.97}(\text{Bi}_2\text{Se}_3)_{1.26}(\text{BiSe})_{0.97}(\text{MoSe}_2)$ containing metallic 1T- MoSe_2 , *Chem. Mater.* **33**, 6403 (2021).
- [30] M. A. Choffel, T. M. Kam, and D. C. Johnson, Substituent effects in the synthesis of heterostructures, *Inorg. Chem.* **60**, 9598 (2021).
- [31] H. Yi, L.-H. Hu, Y. Wang, R. Xiao, J. Cai, D. R. Hickey, C. Dong, Y.-F. Zhao, L.-J. Zhou, R. Zhang, A. R. Richardella, N. Alem, J. A. Robinson, M. H. W. Chan, X. Xu, N. Samarth, C.-X. Liu, and C.-Z. Chang, Crossover from Ising-to Rashba-type superconductivity in epitaxial Bi_2Se_3 /monolayer NbSe_2 heterostructures, *Nat. Mater.* **21**, 1366 (2022).
- [32] M. E. Kamminga, M. Batuk, J. Hadermann, and S. J. Clarke, Misfit phase $(\text{BiSe})_{1.10}\text{NbSe}_2$ as the origin of superconductivity in niobium-doped bismuth selenide, *Commun. Mater.* **1**, 82 (2020).
- [33] G. Mitchson, M. Falmbigl, J. Ditto, and D. C. Johnson, Antiphase boundaries in the turbostratically disordered misfit compound $(\text{BiSe})_{1+\delta}\text{NbSe}_2$, *Inorg. Chem.* **54**, 10309 (2015).
- [34] V. Petříček, I. Cisarova, J. De Boer, W. Zhou, A. Meetsma, G. Wieggers, and S. van Smaalen, The modulated structure of the commensurate misfit-layer compound $(\text{BiSe})_{1.09}\text{TaSe}_2$, *Acta Crystallogr. Sect. B* **49**, 258 (1993).
- [35] B. A. Trump, K. J. T. Livi, and T. M. McQueen, The new misfit compound $(\text{BiSe})_{1.15}(\text{TiSe}_2)_2$ and the role of dimensionality in the $\text{Cu}_x(\text{BiSe})_{1+\delta}(\text{TiSe}_2)_n$ series, *J. Solid State Chem.* **209**, 6 (2014).
- [36] A. Nader, A. Briggs, and Y. Gotoh, Superconductivity in the misfit layer compounds $(\text{BiSe})_{1.10}(\text{NbSe}_2)$ and $(\text{BiS})_{1.11}(\text{NbS}_2)$, *Solid State Commun.* **101**, 149 (1997).
- [37] M. M. Smeller, C. L. Heideman, Q. Lin, M. Beekman, M. D. Anderson, P. Zschack, I. M. Anderson, and D. C. Johnson, Structure of turbostratically disordered misfit layer compounds $[(\text{PbSe})_{0.99}]_1[\text{WSe}_2]_1$, $[(\text{PbSe})_{1.00}]_1[\text{MoSe}_2]_1$, and $[(\text{SnSe})_{1.03}]_1[\text{MoSe}_2]_1$, *Z. Anorg. Allg. Chem.* **638**, 2632 (2012).
- [38] N. Giang, Q. Xu, Y. S. Hor, A. J. Williams, S. E. Dutton, H. W. Zandbergen, and R. J. Cava, Superconductivity at 2.3 K in the misfit compound $(\text{PbSe})_{1.16}(\text{TiSe}_2)_2$, *Phys. Rev. B* **82**, 024503 (2010).
- [39] Q. Lin, M. Smeller, C. L. Heideman, P. Zschack, M. Koyano, M. D. Anderson, R. Kykyneshi, D. A. Keszler, I. M. Anderson, and D. C. Johnson, Rational synthesis and characterization of a new family of low thermal conductivity misfit layer compounds $[(\text{PbSe})_{0.99}]_m(\text{WSe}_2)_n$, *Chem. Mater.* **22**, 1002 (2010).
- [40] A. Chikina, G. Bhattacharyya, D. Curcio, C. E. Sanders, M. Bianchi, N. Lanatà, M. Watson, C. Cacho, M. Bremholm, and P. Hofmann, One-dimensional electronic states in a natural misfit structure, *Phys. Rev. Mater.* **6**, L092001 (2022).
- [41] Q. Yao, D. W. Shen, C. H. P. Wen, C. Q. Hua, L. Q. Zhang, N. Z. Wang, X. H. Niu, Q. Y. Chen, P. Dudin, Y. H. Lu, Y. Zheng, X. H. Chen, X. G. Wan, and D. L. Feng, Charge transfer effects in naturally occurring van der Waals heterostructures $(\text{PbSe})_{1.16}(\text{TiSe}_2)_m$ ($m = 1, 2$), *Phys. Rev. Lett.* **120**, 106401 (2018).
- [42] Z. Song, J. Huang, S. Zhang, Y. Cao, C. Liu, R. Zhang, Q. Zheng, L. Cao, L. Huang, J. Wang, T. Qian, H. Ding, W. Zhou, Y.-Y. Zhang, H. Lu, C. Shen, X. Lin, S. Du, and H.-J. Gao, Observation of an incommensurate charge density wave in monolayer $\text{TiSe}_2/\text{CuSe}/\text{Cu}(111)$ heterostructure, *Phys. Rev. Lett.* **128**, 026401 (2022).
- [43] M. Esters, R. G. Hennig, and D. C. Johnson, Insights into the charge-transfer stabilization of heterostructure components with unstable bulk analogs, *Chem. Mater.* **30**, 4738 (2018).
- [44] M.-X. Wang, P. Li, J.-P. Xu, Z.-L. Liu, J.-F. Ge, G.-Y. Wang, X. Yang, Z.-A. Xu, S.-H. Ji, C. L. Gao, D. Qian, W. Luo, C. Liu, and J.-F. Jia, Interface structure of a topological insulator/superconductor heterostructure, *New J. Phys.* **16**, 123043 (2014).
- [45] G. Mitchson, E. Hadland, F. Göhler, M. Wanke, M. Esters, J. Ditto, E. Bigwood, K. Ta, R. G. Hennig, T. Seyller, and D. C. Johnson, Structural changes in 2D BiSe bilayers as n increases in $(\text{BiSe})_{1+\delta}(\text{NbSe}_2)_n$ ($n = 1-4$) heterostructures, *ACS Nano* **10**, 9489 (2016).
- [46] G. Kresse and D. Joubert, From ultrasoft pseudopotentials to the projector augmented-wave method, *Phys. Rev. B* **59**, 1758 (1999).
- [47] G. Kresse and J. Hafner, *Ab initio* molecular dynamics for liquid metals, *Phys. Rev. B* **47**, 558 (1993).
- [48] G. Kresse and J. Furthmüller, Efficiency of *ab-initio* total energy calculations for metals and semiconductors using a plane-wave basis set, *Comput. Mater. Sci.* **6**, 15 (1996).
- [49] G. Kresse and J. Furthmüller, Efficient iterative schemes for *ab initio* total-energy calculations using a plane-wave basis set, *Phys. Rev. B* **54**, 11169 (1996).
- [50] J. P. Perdew, K. Burke, and M. Ernzerhof, Generalized gradient approximation made simple, *Phys. Rev. Lett.* **77**, 3865 (1996).

- [51] S. Grimme, Semiempirical GGA-type density functional constructed with a long-range dispersion correction, *J. Comput. Chem.* **27**, 1787 (2006).
- [52] See Supplemental Material at <http://link.aps.org/supplemental/10.1103/PhysRevB.109.115112> for details of heterostructure models construction and the comparisons between different choices of DFT methods.
- [53] L. Bengtsson, Dipole correction for surface supercell calculations, *Phys. Rev. B* **59**, 12301 (1999).
- [54] V. Wang, N. Xu, J.-C. Liu, G. Tang, and W.-T. Geng, Vaspkit: A user-friendly interface facilitating high-throughput computing and analysis using VASP code, *Comput. Phys. Commun.* **267**, 108033 (2021).
- [55] Q. Zheng, VASPBANDUNFOLDING, <https://github.com/QijingZheng/VaspBandUnfolding> (2017).
- [56] V. I. Anisimov, J. Zaanen, and O. K. Andersen, Band theory and Mott insulators: Hubbard U instead of Stoner I , *Phys. Rev. B* **44**, 943 (1991).
- [57] J. W. Furness, A. D. Kaplan, J. Ning, J. P. Perdew, and J. Sun, Accurate and numerically efficient r^2 SCAN meta-generalized gradient approximation, *J. Phys. Chem. Lett.* **11**, 8208 (2020).
- [58] W. Tang, E. Sanville, and G. Henkelman, A grid-based Bader analysis algorithm without lattice bias, *J. Phys.: Condens. Matter* **21**, 084204 (2009).
- [59] X. Ni, H. Li, and J.-L. Brédas, Organic self-assembled monolayers on superconducting NbSe₂: interfacial electronic structure and energetics, *J. Phys.: Condens. Matter* **34**, 294003 (2022).
- [60] Y. Liu, P. Stradins, and S.-H. Wei, Van der Waals metal-semiconductor junction: Weak Fermi level pinning enables effective tuning of Schottky barrier, *Sci. Adv.* **2**, e1600069 (2016).
- [61] H. G. Kim and H. J. Choi, Thickness dependence of work function, ionization energy, and electron affinity of Mo and W dichalcogenides from DFT and GW calculations, *Phys. Rev. B* **103**, 085404 (2021).
- [62] P. K. J. Wong, W. Zhang, F. Bussolotti, X. Yin, T. S. Herg, L. Zhang, Y. L. Huang, G. Vinai, S. Krishnamurthi, D. W. Bukhvalov, Y. J. Zheng, R. Chua, A. T. N'Diaye, S. A. Morton, C.-Y. Yang, K.-H. O. Yang, P. Torelli, W. Chen, K. E. J. Goh, J. Ding *et al.*, Evidence of spin frustration in a vanadium diselenide monolayer magnet, *Adv. Mater.* **31**, 1901185 (2019).
- [63] Z.-L. Liu, X. Wu, Y. Shao, J. Qi, Y. Cao, L. Huang, C. Liu, J.-O. Wang, Q. Zheng, Z.-L. Zhu, K. Ibrahim, Y.-L. Wang, and H.-J. Gao, Epitaxially grown monolayer VSe₂: an air-stable magnetic two-dimensional material with low work function at edges, *Sci. Bull.* **63**, 419 (2018).
- [64] Q. Zhang, S. Zhang, B. A. Sperling, and N. V. Nguyen, Band offset and electron affinity of monolayer MoSe₂ by internal photoemission, *J. Electron. Mater.* **48**, 6446 (2019).
- [65] J.-N. Liu, X. Yang, H. Xue, X.-s. Gai, R. Sun, Y. Li, Z.-Z. Gong, N. Li, Z.-K. Xie, W. He, X.-Q. Zhang, D. Xue, and Z.-H. Cheng, Surface coupling in Bi₂Se₃ ultrathin films by screened Coulomb interaction, *Nat. Commun.* **14**, 4424 (2023).
- [66] S. LaShell, B. A. McDougall, and E. Jensen, Spin splitting of an Au(111) surface state band observed with angle resolved photoelectron spectroscopy, *Phys. Rev. Lett.* **77**, 3419 (1996).
- [67] K. Ishizaka, M. S. Bahramy, H. Murakawa, M. Sakano, T. Shimojima, T. Sonobe, K. Koizumi, S. Shin, H. Miyahara, A. Kimura, K. Miyamoto, T. Okuda, H. Namatame, M. Taniguchi, R. Arita, N. Nagaosa, K. Kobayashi, Y. Murakami, R. Kumai, Y. Kaneko *et al.*, Giant Rashba-type spin splitting in bulk BiTeI, *Nat. Mater.* **10**, 521 (2011).